

# Slip statistics of dislocation avalanches under different loading modes

R. Maaß,<sup>1,\*</sup> M. Wraith,<sup>2</sup> J. T. Uhl,<sup>2</sup> J. R. Greer,<sup>1,3</sup> and K. A. Dahmen<sup>2</sup>

<sup>1</sup>*California Institute of Technology, Division of Engineering and Applied Sciences, 1200 East California Boulevard, Pasadena, California 91125, USA*

<sup>2</sup>*University of Illinois at Urbana-Champaign, Department of Physics, 1110 West Green Street, Urbana, Illinois 61801, USA*

<sup>3</sup>*Kavli Nanoscience Institute, California Institute of Technology, Pasadena, California 91125, USA*

(Received 12 May 2014; revised manuscript received 28 October 2014; published 14 April 2015)

Slowly compressed microcrystals deform via intermittent slip events, observed as displacement jumps or stress drops. Experiments often use one of two loading modes: an increasing applied stress (stress driven, soft), or a constant strain rate (strain driven, hard). In this work we experimentally test the influence of the deformation loading conditions on the scaling behavior of slip events. **It is found that these common deformation modes strongly affect time series properties, but not the scaling behavior of the slip statistics when analyzed with a mean-field model. With increasing plastic strain, the slip events are found to be smaller and more frequent when strain driven, and the slip-size distributions obtained for both drives collapse onto the same scaling function with the same exponents.** The experimental results agree with the predictions of the used mean-field model, linking the slip behavior under different loading modes.

DOI: [10.1103/PhysRevE.91.042403](https://doi.org/10.1103/PhysRevE.91.042403)

PACS number(s): 62.20.F-, 62.25.-g, 61.46.Hk, 81.07.-b

## I. INTRODUCTION

Plastic deformation of crystals proceeds intermittently via discrete bursts, or slip events, of a broad range of sizes. Typically, the deformation in both experiments and modeling occurs under two distinctly different loading conditions, which are force controlled (soft), and displacement controlled (hard). For soft loading conditions, the compressive stress is slowly increased at a prescribed rate. For hard loading conditions, a fixed compressive strain rate is imposed. In this work, we experimentally test the theoretically predicted dependency on the loading conditions of the time series properties of the slip events, as well as the scaling behavior of the slip statistics.

The process of intermittent and stochastic changes of an evolving driven system has been studied intensely in the past decades. Prominent examples are the intermittency of energy dissipation in magnetism, superconductivity, earthquakes, and, for example, friction [1]. Despite the fact that the scales of their events are many orders of magnitude different, **the statistical nature of the discrete events exhibits similar probability distributions.** Yet another example of a discretely evolving system is a plastically flowing crystal, where the underlying dislocation structure reorganizes from one critical state to another. While early stress-strain evidence exists that plastic flow is intermittent [2], acoustic emission (AE) is readily used to record the crackling noise from deforming crystals [3–8]. In such experiments, the AE amplitude reveals power-law scaling indicative of the scale-free nature of plastic deformation. This can also be observed by directly tracing the magnitude of crystallographic slip events (dislocation avalanches) [9–12] or the corresponding avalanche velocity [13,14] upon straining of micron-sized single crystals.

Even though power-law scaling is consistently observed in critically evolving systems, the exponents from different

experiments have been shown to be difficult to compare [15,16] because of differing loading conditions. Consequently, the effects of loading mode and boundary conditions in avalanche-mediated transitions have become a topic of increasing interest for systems with power-law dynamics [16–20]. Earlier studies either focus on the comparison between simulations and experiment for one given type of loading or boundary conditions [3], or make comparisons for different loading or boundary conditions entirely based on simulations [16–18,21]. For example, in the specific case of an evolving dislocation network, reflecting pinning-depinning dynamics, dislocation-dynamics simulations [21] have indicated that **the scaling behavior of the avalanche statistics, quantified, for example, by the avalanche size distribution, should remain unaffected by both internal variables, such as material and crystal structure, as well as by the imposed deformation mode.** The latter implies insensitivity of the statistics to how the dislocation structure is being driven and whether it is allowed to relax intermittently by differences that depend on how the external stress is imposed. This is particularly interesting, because dislocation networks are known to evolve with strain from a low density and energy configuration to highly complex and hierarchical dislocation structures. Until today, a direct comparison between theoretical predictions and experimental data is lacking, and in particular no experimental study has tested whether universality across hard and soft loading conditions exists for evolving dislocation networks.

Here, we therefore investigate the slip-size magnitudes of quasistatically deforming microcrystals under two very different loading conditions: stress-driven (soft) and strain-driven (hard) loading. We compute the slip statistics for sufficiently slow driving speed, that is as close as possible to the adiabatic limit. In order to compare experimental data from different driving modes, a scaling collapse method is introduced. Applying a mean-field model, all experimental data from stress- and strain-driven loading can be collapsed onto a universal scaling function, directly proving the theoretical predictions. Furthermore, we find that the time series properties of dislocation avalanches near failure are markedly

\*Present address: University of Göttingen, Institute for Materials Physics, Friedrich-Hund-Platz 1, 37077 Göttingen, Germany.

<sup>†</sup>Corresponding authors: [rmaass@illinois.edu](mailto:rmaass@illinois.edu), [dahmen@illinois.edu](mailto:dahmen@illinois.edu)

different for the two loading conditions, a finding that may be of immediate relevance for nondestructive testing and failure prediction.

## II. MODEL ASSUMPTIONS AND EXPERIMENTAL DETAILS

Before turning our attention to the experiments and their comparison to theory, we first outline the used mean-field model, its predictions, and some experimental details. The employed model [22,23] assumes that the material has weak spots, e.g., pinned dislocations in the crystal. These weak spots slip whenever the local stress at the spot exceeds a random threshold, causing it to displace until the stress is reduced to some arrest stress. All weak spots are elastically coupled such that a slipping spot can trigger other spots to slip, leading to a slip avalanche. The model has been solved analytically in the mean-field theory (MFT) approximation, which assumes that the interactions have infinite range, i.e., they do not decay with distance [22,23]. MFT exactly predicts the scaling behavior of the slip statistics in three dimensions as described below, and agrees well with discrete dislocation-dynamics simulations [24–26] and experiments [27]. In the following, we compute the slip statistics for sufficiently slow driving in the quasistatic limit.

In the absence of hardening, the model predicts that the probability density distribution  $D(S, F)$  of slip sizes  $S$  occurring at an applied force  $F$ , follows a power law with a force-dependent maximum size cutoff  $S_{\max} = c(F_c - F)^{-1/\sigma}$  as

$$D(S, F) \sim S^{-\tau} f_s[S(F_c - F)^{\frac{1}{\sigma}}] = S^{-\tau} f_s(cS/S_{\max}). \quad (1)$$

Here  $\tau = 3/2$ ,  $\sigma = 1/2$ , and  $f_s(x) = e^{-Ax}$  are the detail-independent “universal” exponents and scaling function, respectively.  $F_c$  is a critical force and model parameter, above which the material cannot sustain any load, and we further discuss its meaning in the Appendix.  $A$  and  $c$  are material-dependent parameters.

Using the well known method of scaling collapses [28], we introduce a general scaling collapse that uses the average avalanche sizes for different displacement windows as the tuning variable rather than the stress itself, which enables the comparison of experiments with different driving modes or unknown tuning parameter values. Equation (1) predicts that the average avalanche size  $\langle S \rangle(F) \equiv \int_0^\infty S D(S, F) dS$  scales with applied force as  $\langle S \rangle(F) \sim (F_c - F)^{(\tau-2)/\sigma}$ , as shown in Ref. [22], or equivalently  $F_c - F \sim \langle S \rangle^{\sigma/(\tau-2)}$ . Substituting  $\langle S \rangle^{\sigma/(\tau-2)}$  for  $(F_c - F)$  in Eq. (1) then gives a scaling form for the avalanche size distribution in terms of the average avalanche size  $\langle S \rangle(F) \equiv \langle S \rangle$  for a small bin in force  $F$ :

$$D(S, \langle S \rangle) \sim \langle S \rangle^{\tau/(\tau-2)} g_s(S \langle S \rangle^{1/(\tau-2)}). \quad (2)$$

The scaling function  $g_s(x) = x^{-\tau} \exp(-Bx)$  is universal, while  $B$  is a material-dependent parameter. Equation (2) also yields the scaling form for the complementary cumulative distribution function (CDF) [22,27]  $C(S, \langle S \rangle) \equiv \int_S^\infty D(S', \langle S \rangle) dS'$ , which gives the relative number of avalanches larger than  $S$  that occur in a stress bin with the average avalanche size  $\langle S \rangle$ :

$$C(S, \langle S \rangle) \sim \langle S \rangle^{[(\tau-1)/(\tau-2)]} g_c(S \langle S \rangle^{1/(\tau-2)}), \quad (3)$$

where  $g_c(x) = \int_x^\infty dt e^{-Bt} t^{-\tau}$  is a universal scaling function and  $\tau = 3/2$  in MFT. In the quasistatic limit,  $C(S, \langle S \rangle)$  is predicted to be identical for both stress-driven and strain-driven deformation, such that the exponents and scaling functions of the avalanche size distribution are the same regardless of the deformation mode or how the dislocation ensemble is driven. This model prediction will be tested in the following with experimental data, first by conducting the appropriate collapse, using  $\tau = 3/2$ , followed by fitting the collapsed data to Eq. (3). Equation (3) is more general than Eq. (1) and applies to materials with or without hardening [22]. Additional scaling forms are discussed in the Appendix.

In order to experimentally test the theoretical predictions, uniaxial microcompression tests were conducted on cylindrical [001]-oriented Au single crystals with diameters of 1  $\mu\text{m}$  (seven crystals), 3  $\mu\text{m}$  (nine crystals) and 5  $\mu\text{m}$  (eight crystals), with a nominal aspect ratio of 3 and a side wall taper angle smaller than 1.2°. The crystals were compressed in a Hysitron nanoindenter either using a strain-driven (displacement controlled, equivalent to hard) or a stress-driven (force controlled, equivalent to soft) deformation mode [29]. In the following, displacement represents the platen position during loading, and by “force” we mean the value applied by the device onto the crystal. Both displacement (equivalent to strain) and force (equivalent to stress, quantified as engineering stress [14,30]) were acquired at a rate of 60 Hz and are measured with subnanometer and subnanonewton precision. The samples were prepared by following a multistep annular focused ion beam (FIB) methodology used in earlier work [14].

## III. RESULTS AND DISCUSSION

Figure 1(a) depicts a typical force-displacement data set for a test conducted in each deformation mode. Despite different force levels during plastic flow for different crystal sizes, the data in Fig. 1 are representative for all sample diameters investigated in this study. In both strain-driven and stress-driven compression the flow response is characterized by a series of discrete displacement jumps that reflect slip events (dislocation avalanches [13,14]). During a slip event the true plastic strain rate is larger than the nominally applied strain rate. The two deformation modes differ significantly in the way they drive the evolving underlying dislocation structure and how intermediate internal stress states are sampled. For force-displacement data that span the same total displacement, on average the slip events have larger displacements in the stress-driven mode than in the strain-driven mode. Also, in the strain-driven data one finds larger overall force increments per unit displacement than in the stress-driven mode. Both effects are explained by the conditions imposed on the sample in each mode. Each displacement jump in both strain-driven and stress-driven deformation is consisting of a forward surge in displacement,  $S$ , and a simultaneously occurring force drop,  $\Delta F$ , that leads to a stress relaxation of the deforming sample. A comparison for a slip event (dislocation avalanche) obtained under stress-driven and strain-driven loading conditions is shown in Figs. 1(b) and 1(c), respectively. The applied force, and thus stress, is kept approximately constant during slip events in the stress-driven mode. In contrast, strain-driven compression is characterized by a force decrease (stress drops)

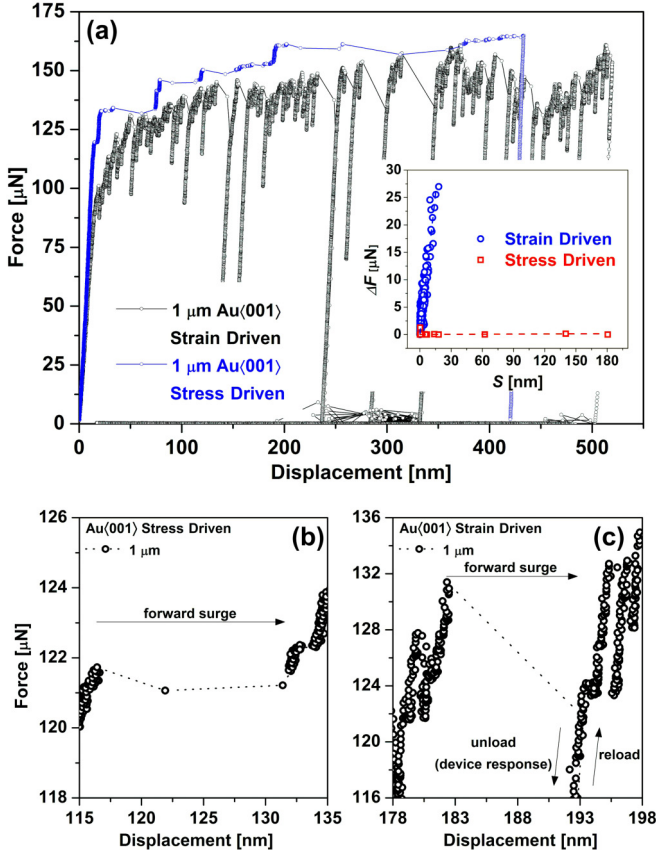


FIG. 1. (Color online) (a) Force-displacement curves for two  $1\text{-}\mu\text{m}$  Au(001) microcrystals deformed with different loading conditions ( $0.5\text{ nm/s}$  for strain driven, and  $0.4\mu\text{N/s}$  for stress driven). The inset in (a) shows the correlation between slip-induced force-drop magnitude,  $\Delta F$ , and slip-size magnitude,  $S$ . Linear fits are displayed by dashed lines. Close-up views on a slip event during stress-driven compression (b) and strain-driven compression (c) demonstrate the different slip dynamics in terms of  $\Delta F$ .

during and after the discrete slip events [Fig. 1(c)]. The reason is that the slipping crystal and the device are acting as two springs in series, which relax during the slip event, thereby reducing the stored elastic energy. The inset in Fig. 1(a) displays the correlation between force drop and slip size, both evaluated between the beginning and end of the slip event, for microcrystals with a diameter of  $1\text{ }\mu\text{m}$  tested in strain-driven and stress-driven mode. In both cases, the data falls on a linear trend, but with markedly different maximum  $S$  values and  $\Delta F - S$  slopes. The  $\Delta F - S$  slopes of the dashed linear fits differ by a factor of  $\sim 2200$  ( $1.7\text{ }\mu\text{N/nm}$  for strain control,  $7.7 \times 10^{-4}\text{ }\mu\text{N/nm}$  for stress control). Considering the sample and machine as two serial springs, where the axial transducer stiffness is  $\sim 10^2\text{ N/m}$ , and the sample has an axial stiffness of  $\sim 11\text{ }000\text{ N/m}$ , it is clear that the dominant contribution to the apparent stiffness for the strain-driven data originates from the much more compliant transducer. The effective  $\Delta F - S$  slope in strain-driven deformation amounts to  $\sim 1700\text{ N/m}$ , which only can be understood when considering the efficient and fast ( $78\text{ kHz}$ ) feedback loop of the device, artificially stiffening the system [29]. For stress-driven testing the assumption of two springs in series does not apply.

Rather, the feedback of the device produces an amplified soft response. Apart from some exceptions, the stress drop magnitude in stress-driven deformation generally amounts to  $\sim 0.5\text{ }\mu\text{N}$ , whereas strain-driven data mainly lie above  $1\text{ }\mu\text{N}$ .

When the device-controlled unload after the slip event in strain-driven deformation is complete, a linear reloading segment follows a slip event [Fig. 1(c)]. Examples of such can be seen in Fig. 1(a) where the elastic reloading segments occur at the displacements of  $\sim 240$ ,  $280$ , and  $335\text{ nm}$ . In contrast, under stress-driven deformation, the stress cannot be lowered during slip events because the applied force is kept fixed during the slip events within the limits of the instrumental capabilities. Thus, a strain-driven system is effectively much stiffer than a stress-driven system, preventing the spanning avalanche from growing. Successive slip events that would be separate in strain-driven compression may be forced to merge in stress-driven deformation. Consequently the slip frequency per force increase is higher in strain-driven than in stress-driven compression. Similar effects have been observed in other systems such as spin models with quenched disorder [17]. A discussion on the stiffness, the instrumental assembly, and different deformation modes of the nanoindenter used in this study is presented in detail in Ref. [29].

Experiments were conducted probing three sample sizes over a range of applied rates:  $0.4 - 3\text{ nm s}^{-1}$  in strain-driven mode and  $0.3 - 2\text{ }\mu\text{N s}^{-1}$  in stress-driven mode. The extent of each avalanche is extracted from the displacement versus time data, following a custom procedure [9,14,27]: a numerical derivative of the displacement versus time data yields the platen velocity  $v$  during the forward surge of the sample-device interface for both compression modes. We set a conservative threshold velocity of  $\langle v \rangle + 2\sigma_v$ , with  $\langle v \rangle$  being the average displacement velocity, and  $\sigma_v$  the standard deviation. We denote the start of an avalanche when the platen velocity first exceeds the prescribed rate, and its end when the displacement velocity subsequently drops below this threshold. The slip size  $S$  is defined as the increase in displacement observed from the start to the end of each avalanche. Representative for the data obtained from the different crystal sizes, Fig. 2 displays the stress-integrated complementary cumulative distributions  $C_{\text{int}}(S)$ , which includes all slip sizes from the entire stress-strain curve of the  $1\text{-micron}$ -large crystals. Further details on the stress-integrated scaling laws can be found in the Appendix. The stress-integrated distributions  $C_{\text{int}}(S)$  for both deformation modes align well with the power-law exponent  $-1$  given by the mean-field model, and, as discussed above, stress-driven deformation produces larger avalanche sizes than strain-driven deformation. A related effect of merged avalanches has been observed for increased applied strain rates [12,27].

For our comparison between experiments and theory, we focus on data obtained for the compression of  $3\text{-}\mu\text{m}$ -diameter crystals at the slowest possible rates,  $0.4\text{ nm/s}$  (strain driven) and  $0.3\text{ }\mu\text{N/s}$  (stress driven), which corresponds to a nominal strain rate of  $\sim 10^{-5}\text{ s}^{-1}$ . These are chosen to attain as close to quasistatic conditions as possible, to mimic the assumptions of the MFT model, and to also exemplify the results of the other crystal sizes. The stress rate of the force-controlled deformation was chosen such that the true plastic strain rate beyond the elastic limit attained values in the range between



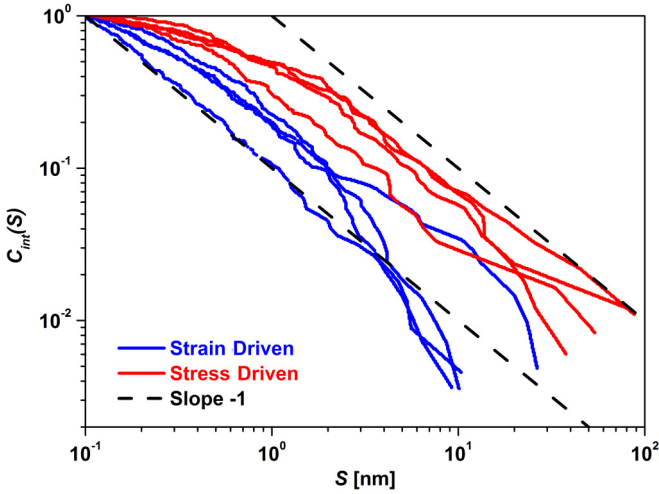


FIG. 2. (Color online) Stress-integrated complementary cumulative distributions  $C_{\text{int}}(S, F_{\text{max}})$  for the  $1\text{-}\mu\text{m}$ -sized crystals. The slope of  $-1$  is the predicted exponent for  $C_{\text{int}}(S, F_{\text{max}})$ . The red curves are from stress-driven experiments, and the blue curves are from strain-driven experiments. The shift to the right of the stress-driven experiments results from the fact that stress-driven conditions produce effectively larger slips.

0.6 and 0.2 nm/s in segments where no resolvable slip event occurred. Within the experimentally controllable means the true plastic rates in both considered deformation modes are therefore comparable. The complementary cumulative distribution functions (CDFs)  $C(S, \langle S \rangle)$  of the collected slip sizes  $S$  are shown in Fig. 3. Different colors denote CDFs for stress bins with different average avalanche size  $\langle S \rangle$ . Figs. 3(a) and 3(b) shows that  $C(S, \langle S \rangle)$  follows the model prediction from Eq. (3) very well for both deformation modes, because the experimental data describe the distribution as given by the CDF of the model. We note that a larger number of data points would be desirable in order to improve the distributions even further. The insets show the scaling collapse obtained via a fitting procedure with the mean-field exponent ( $\tau = 3/2$ ), which supports the predicted scaling function of Eq. (3). Figure 3(c) demonstrates that the data for stress-driven compression collapse onto those for strain-driven compressions. The collapsed data sets not only overlay one another, but they also follow the scaling function predicted by MFT, which was fit to the entire experimental data depicted in Fig. 3(c). Both the constant  $B$  from Eq. (3) and the integration constant  $A$  of  $g_c(x)$  are indicated in Fig. 3(c). The slight deviations, primarily seen for stress-driven data, have three main reasons: (i) less-than-perfectly quasistatic conditions and (ii) the statistically smaller data set, and (iii) finite size effects arising for large events amplified by the soft stress-driven mode. Despite these issues, and also the limited amount of experimental data (ca. 1000 experimental slip events are contained in the analysis of Fig. 3), good support for the earlier described model predictions are found—a remarkable result considering the simplifications made by the theory. The stress-binning procedure is described in the Appendix.

Since the values of the scaling exponents and the scaling function of the collapse agree well with the corresponding

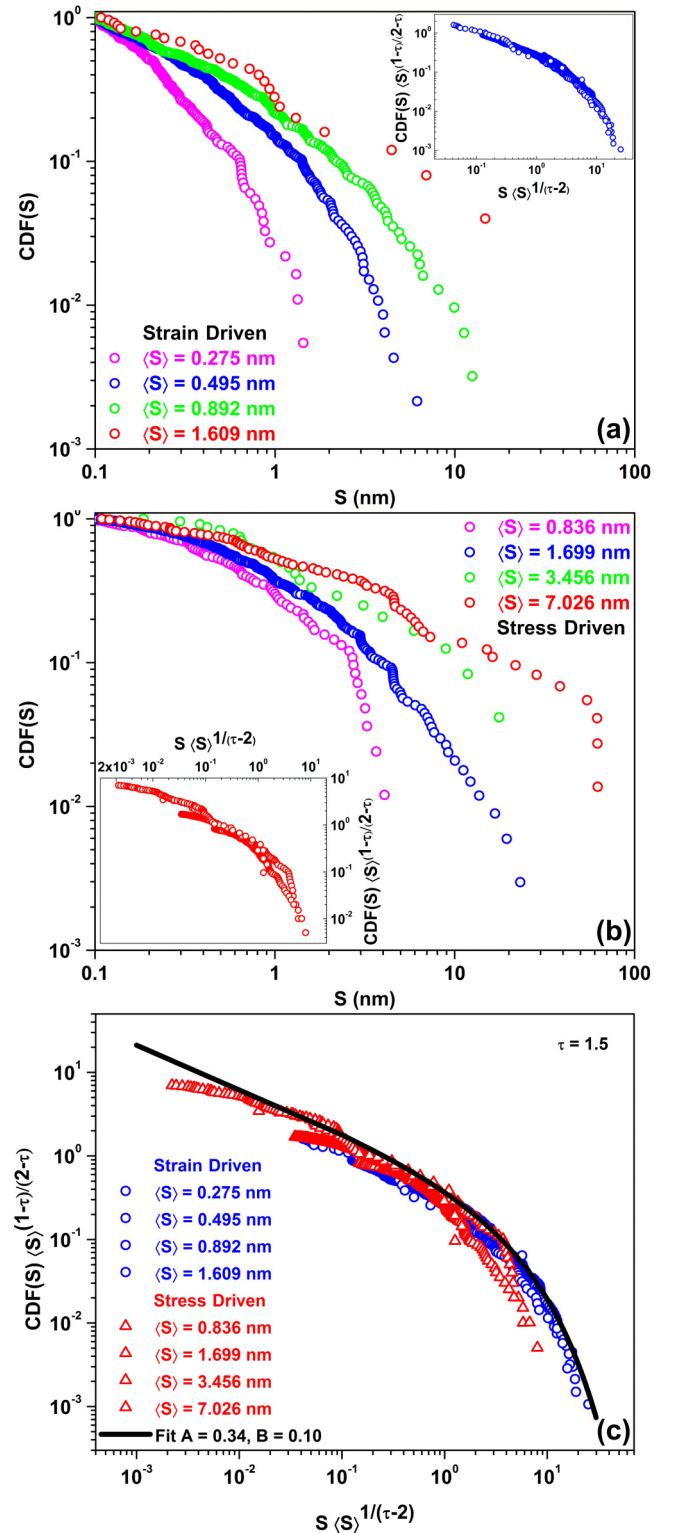


FIG. 3. (Color online) Complementary cumulative avalanche size distributions from quasistatic compressions of  $3\text{-}\mu\text{m}$  Au microcrystals. The colors correspond to different stress bins with different values for the average avalanche size ( $\langle S \rangle$ ); the insets show scaling collapses according to Eq. (3), using the mean-field exponents (a) for strain-driven compression at  $0.4\text{ nm/s}$ , (b) for stress-driven compression at  $0.3\text{ }\mu\text{N/s}$ , (c) scaling collapse for strain driven (blue circles) and stress driven (red triangles). The black curve corresponds to the mean-field scaling function.

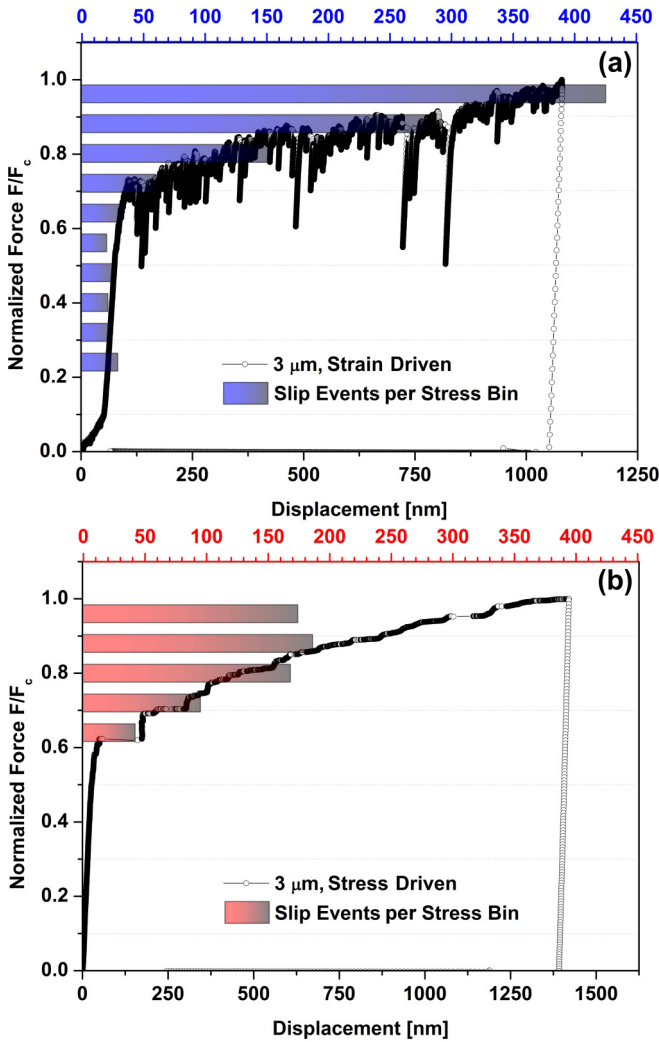


FIG. 4. (Color online) Force versus displacement for typical experiments on 3- $\mu\text{m}$ -diameter Au crystals (a) for strain-driven compression at 0.4 nm/s, (b) for stress-driven compression at 0.3  $\mu\text{N/s}$ . The histograms represent the slip frequency, which is the number of avalanche events within each force bin. The increase in the slip frequency with stress is more pronounced for strain-driven than for stress-driven compressions. In the strain-driven conditions the slip frequency grows exponentially with force as predicted by the model. The upper  $x$  axes indicate the number of events per stress bin.

mean-field predictions applied to our experimental data for two different loading conditions, it is clear that the scaling behavior of the slip statistics is universal beyond the drive of the critically evolving dislocation network. In combination with earlier investigations [9,10,27], a picture emerges where the experimental evidence shows that the power-law statistics are the same for small fcc and bcc crystals, crystal orientation, crystal size, applied deformation rate, and as investigated here, for both soft and hard imposed conditions. This is interesting as viewed in the context of the different strength-size scaling of small-scale fcc and bcc crystals [31], which implies that the underlying strengthening mechanisms are different. Yet, the slip magnitude statistics reveal no noticeable difference across so far all tested conditions and parameters, suggesting that the collective dislocation event close to criticality is insensitive

to the thermally activated mechanisms that govern the size-dependent strength scaling.

In contrast, Fig. 4 shows that time series properties, such as the slip frequency and its variation with force, strongly depend on the experimental deformation mode. The histogram bins in Fig. 4 were obtained using linear binning in applied force at intervals of  $0.1 F/F_c$  and centered at uneven multiples of 0.05. As outlined in more detail in the Appendix,  $F_c$  is a model parameter that represents the force at failure for the studied system. Obviously, a stress as high as  $F_c$  cannot be reached in the experiments conducted here. That is why in this work  $F_c$  was approximated by the maximum force in each loading curve. Figure 4(a) demonstrates that for strain-driven deformation the slip frequency increases strongly with the applied force, while for stress-driven deformation [Fig. 4(b)] such increase is marginal. This holds true irrespective of the fact that higher plastic displacements were achieved in force-controlled deformation. It also holds true if only the plastic strain regime is considered.

In fact, for strain-driven compression the number of slip events per bin increases exponentially with stress, with a decay constant of  $0.79 \pm 0.004$  and a fitting coefficient  $R^2 = 0.998$ . Slip events are observed down to lower normalized force values than for stress-driven compressions. The low initial slope in the elastic regime below  $0.1 F/F_c$  in the stress-strain data shown in Fig. 4(a) is a typical signature of commonly observed indenter-to-sample alignment [30], and we have chosen not to include any such events in the slip frequency analysis of Fig. 4(a) in order to only compare the strain- and force-driven data obtained after linear loading sets in.

The exponential increase of the slip frequency with stress for strain-driven deformation is consistent with our model predictions. Equation (1) states that slip events at higher stresses become larger under stress-driven conditions. Since, as described above, these larger events are continuously broken down into smaller slip sizes in strain-driven deformation, the slip triggering rate has to increase with stress. The exact number depends on the stiffness of the material and the measurement instrument, but the trend is expected to be similar across many different materials. The exponential dependence of the slip frequency on the stress follows from the model for the commonly assumed Weibull distribution of weak spot strengths with exponentially decaying tails.

#### IV. SUMMARY

In this work we have made an experimental investigation on effects of loading conditions on the slip statistics obtained from plastically deforming microcrystals, with the aim at testing the theoretical prediction that scaling exponents for intermittent dislocation plasticity are insensitive to how the dislocation structure is externally driven. To this end, we have compared the slip statistics from dislocation avalanches under soft (stress driven) and hard (strain driven) deformation conditions. The comparison of experimental data with predictions of a simple mean-field model shows that the scaling behavior of the slip avalanche statistics of a dynamically changing dislocation network is universal across both deformation modes for the slowest accessible applied rates and low device stiffness. In contrast, time series properties such as the slip sizes and

the stress-dependent slip frequency depend markedly on the loading conditions, where the increase in slip frequency is exponentially growing with plastic strain under strain-driven deformation, and a much slower increase is observed under stress-driven conditions. That means by studying the avalanche rate change of plastically deforming crystals, as well as other systems exhibiting scale-free crackling noise, it is possible to differentiate between the mode of the externally applied drive. The obtained results are expected to apply to the deformation of many driven inhomogeneous systems that evolve critically, and they may be useful for materials testing applications.

## ACKNOWLEDGMENTS

The authors thank James Antonaglia, P. M. Derlet, and Nir Friedman for fruitful discussions. The authors thank the SURF program at Caltech for providing funding and the opportunity to contribute to this project. R.M. is grateful for the financial support of the Alexander von Humboldt Foundation during his stay at Caltech, as well as to his host G. M. Pharr. J.R.G. is thankful for the financial support of the Office of Naval Research (ONR Grant No. N000140910883). K.A.D. thanks MGA and NSF for funding through NSF Grant No. DMR 1005209 and NSF Grant No. DMS1069224, and the Kavli Institute of Theoretical Physics (KITP) at UCSB for hospitality and support through Grant No. NSF PHY11-25915.

## APPENDIX A: STRESS-INTEGRATED DISTRIBUTIONS

The multivariate nature of the distribution  $D(S, F)$  can be integrated with respect to the force from zero up to some maximum force  $F_{\max} < F_c$ , yielding

$$D_{\text{int}}(S, F_{\max}) \sim S^{-(\tau+\sigma)} f_{\text{int}}[S(F_c - F_{\max})^{-1/\sigma}]. \quad (\text{A1})$$

$f_{\text{int}}$  is an exponentially decaying scaling function, and  $F_c$  is a critical force, above which the material cannot sustain any load and should be seen as a model parameter. We note that for finite systems sizes,  $F_c$  will reflect sample-dependent fluctuations, and the distribution of  $F_c$  would have a size-dependent width. If  $F_c - F_{\max}$  is chosen to be small, as in our case, then the power-law dominates for the broad range of avalanche sizes  $0 < S < (F_c - F_{\max})^{-1/\sigma}$  with an exponent of  $\tau + \sigma = 2$  predicted by the mean-field theory model described in the main text.

Integrating with respect to the force up to  $F_{\max} = F_c$  yields a pure power law  $D_{\text{int}}(S, F_c) \sim S^{-(\tau+\sigma)}$ . This power-law distribution provides less information than the stress-dependent distribution in Eq. (A1). The reason is that  $\tau$  and  $\sigma$  cannot be separately determined from this power law alone, where the stress dependence is fully integrated out. On the other hand the stress-integrated distribution  $D_{\text{int}}(S, F_c)$  usually has better statistics because it takes into account all measured avalanches for the full stress range, while the stress-dependent distribution only takes into account a fraction of the avalanches for a smaller stress range, and therefore has larger statistical fluctuations. Plotting  $D_{\text{int}}(S, F_c)$  and comparing it with the predicted power law  $S^{-(\tau+\sigma)}$  constitutes a strong test of the theory.

The statistical fluctuations can be reduced even further by plotting the corresponding complementary cumulative distribution function (CDF), which is predicted to scale as  $C_{\text{int}}(S) \sim S^{-(\tau+\sigma-1)}$ ; see main text.

Our mean-field model predicts  $\tau + \sigma = 2$ , so that the predicted power-law decay exponent on the CDF  $C_{\text{int}}(S)$  should be  $-1$ , i.e.,  $C_{\text{int}}(S) \sim 1/S$  in mean-field theory.

In Fig. 2 a set of four strain-driven and stress-driven experimental data sets  $C_{\text{int}}(S, F_{\max})$  for  $1\text{-}\mu\text{m}$ -sized crystals are shown together with theoretical lines of slope  $-1$ . By integrating Eq. (A1) over avalanche size from  $S$  to infinity we obtain

$$C_{\text{int}}(S, F_{\max}) \sim S^{-(\tau+\sigma-1)} g_{\text{int}}[S(F_c - F_{\max})^{1/\sigma}]. \quad (\text{A2})$$

Here  $g_{\text{int}}$  is another exponentially decaying scaling function that is responsible for the slight bend downwards of the distributions for large avalanche sizes  $S$ .

## APPENDIX B: BINNING THE AVALANCHE DATA IN $\langle S \rangle$ :

The cumulative distributions shown in the main paper corresponding to different  $\langle S \rangle$  values are obtained from collecting slip sizes for different bins in time or displacement. For nominally identical  $3\text{-}\mu\text{m}$  microcrystals, these bins are indicated by different colors in Fig. 5(a) for displacement-controlled, and in Fig. 5(b) for force-controlled compression. Only data from the plastic regime is shown and the force-displacement curves of the different specimen have been shifted relative to each other for clarity. Large gaps in the stress-driven curves in Fig. 5(b) are due to large slips (sudden jumps in displacement) during plastic deformation.

It is clear that in the stress-driven mode both stress and strain are monotonically increasing in time; i.e., the data in the  $(n+1)$ st bin is at larger stress and displacement values than the data in the  $n$ th bin (where the index  $n$  increases with time). Therefore stress binning of stress-controlled deformation can always be transferred into time binning, without any loss of generality.

Similarly, in the strain-driven mode, the displacement is monotonically increasing in time, so time binning will work there as well. Note, however, that time, force, or stress bins in the strain-driven mode may result in a much larger number of slip displacements for bins at higher strain, as shown in the main paper. This is resulting from the possibility of effectively zero hardening (or softening) with increasing deformation. With hardening, we refer to the derivative of the upper envelope of the stress-strain curve, i.e., its increase in stress per increase in displacement. In the limit of an elastic-perfectly-plastic material, all slip events would fall into a single and very narrow stress bin due to a constant stress level throughout plastic flow. Parts of the force-displacement curve in Fig. 1 display such regimes with effectively zero hardening or softening after an initial hardening regime.

The question emerges how stress and/or force binning can be done adequately without placing a large part of the slips arising at the later stage of deformation into just one bin. We find that the force-displacement curve has sections (“arches”) where the curve starts with a steep slope (high apparent hardening rate, far from criticality), after which the hardening rate becomes lower, which we call more critical. Subsequently a large event occurs, and then the system returns to being far from criticality—similar to the mechanism discussed by Papanikolaou *et al.* [32]. Here, we calculate  $\langle S \rangle$  for each such arch and then group the avalanches in those arched sections

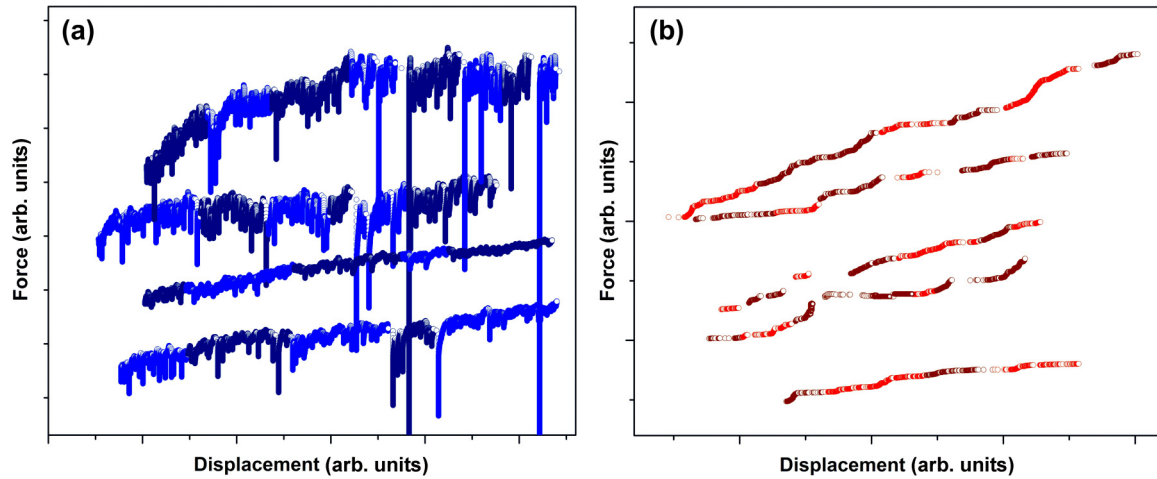


FIG. 5. (Color online) Plastic part of the force-displacement data for all-3- $\mu\text{m}$  microcrystals deformed in both strain-driven [0.4 nm/s, Fig. 5(a)] and stress-driven [0.3  $\mu\text{N/s}$ , Fig. 5(b)] steering mode. The alternating colored parts of the curves represent different displacement bins that are later grouped according to their corresponding  $\langle S \rangle$  values into different  $\langle S \rangle$  bins. Large gaps in the stress-driven curves in Fig. 5(b) are due to large slip events during plastic deformation.

together so that have roughly the same average slip sizes  $\langle S \rangle$ . The resulting slip-size distributions for different  $\langle S \rangle$ -values, are used for the scaling collapses in the main paper [Fig. 3(c)]. This analysis does not require prior knowledge of the tuning parameter (stress or strain), and it allows us to perform the identical analysis for stress-driven and strain-driven loading

conditions. The idea is to define suitable displacement bins in both cases, to calculate  $\langle S \rangle$  for each bin, and then to form new histograms of the avalanches that came from bins with the same  $\langle S \rangle$  value. This method is generally applicable to systems where the driving parameter is either not known or where we need to compare systems with different driving parameters.

- 
- [1] D. S. Fisher, *Phys. Rep.* **301**, 113 (1998).
  - [2] R. F. Tinder and J. P. Trzil, *Acta Metall.* **21**, 975 (1973).
  - [3] M. C. Miguel, A. Vespignani, S. Zapperi, J. Weiss, and J. R. Grasso, *Nature* **410**, 667 (2001).
  - [4] G. Ananthakrishna, S. J. Noronha, C. Fressengeas, and L. P. Kubin, *Phys. Rev. E* **60**, 5455 (1999).
  - [5] J. Weiss, T. Richeton, F. Louchet, F. Chmelik, P. Dobron, D. Entemeyer, M. Lebyodkin, T. Lebedkina, C. Fressengeas, and R. J. McDonald, *Phys. Rev. B* **76**, 224110 (2007).
  - [6] J. Weiss and D. Marsan, *Science* **299**, 89 (2003).
  - [7] T. Richeton, P. Dobron, F. Chmelik, J. Weiss, and F. Louchet, *Mater. Sci. Eng. A* **424**, 190 (2006).
  - [8] T. Richeton, J. Weiss, F. Louchet, P. Dobron, and F. Chmelik, *Kovove Mater.* **45**, 149 (2007).
  - [9] D. M. Dimiduk, C. Woodward, R. LeSar, and M. D. Uchic, *Science* **312**, 1188 (2006).
  - [10] M. Zaiser, J. Schwerdtfeger, A. S. Schneider, C. P. Frick, B. G. Clark, P. A. Gruber, and E. Arzt, *Philos. Mag.* **88**, 3861 (2008).
  - [11] S. Brinckmann, J.-Y. Kim, and J. R. Greer, *Phys. Rev. Lett.* **100**, 155502 (2008).
  - [12] S. Papanikolaou, D. M. Dimiduk, W. Choi, J. P. Sethna, M. D. Uchic, C. F. Woodward, and S. Zapperi, *Nature* **490**, 517 (2012).
  - [13] R. Maass, P. M. Derlet, and J. R. Greer, *Small* **11**, 341 (2015).
  - [14] R. Maass, P. M. Derlet, and J. R. Greer, *Scr. Mater.* **69**, 586 (2013).
  - [15] G. Durin and S. Zapperi, *Phys. Rev. Lett.* **84**, 4705 (2000).
  - [16] L. Zhang, E. K. H. Salje, X. Ding, and J. Sun, *Appl. Phys. Lett.* **104**, 162906 (2014).
  - [17] F.-J. Perez-Reche, L. Truskinovsky, and G. Zanzotto, *Phys. Rev. Lett.* **101**, 230601 (2008).
  - [18] B. Tadic, *Phys. Rev. Lett.* **77**, 3843 (1996).
  - [19] G. Bertotti, G. Durin, and A. Magni, *J. Appl. Phys.* **75**, 5490 (1994).
  - [20] F. J. Perez-Reche, B. Tadic, L. Manosa, A. Planes, and E. Vives, *Phys. Rev. Lett.* **93**, 195701 (2004).
  - [21] F. F. Csikor, C. Motz, D. Weygand, M. Zaiser, and S. Zapperi, *Science* **318**, 251 (2007).
  - [22] K. A. Dahmen, Y. Ben-Zion, and J. T. Uhl, *Phys. Rev. Lett.* **102**, 175501 (2009).
  - [23] K. A. Dahmen, Y. Ben-Zion, and J. T. Uhl, *Nat. Phys.* **7**, 554 (2011).
  - [24] G. Tsekenis, J. T. Uhl, N. Goldenfeld, and K. A. Dahmen, *Europhys. Lett.* **101**, 36003 (2013).
  - [25] G. Tsekenis, N. Goldenfeld, and K. A. Dahmen, *Phys. Rev. Lett.* **106**, 105501 (2011).
  - [26] P. M. Derlet and R. Maass, *Modell. Simul. Mater. Sci. Eng.* **21**, 035007 (2013).
  - [27] N. Friedman, A. T. Jennings, G. Tsekenis, J.-Y. Kim, M. Tao, J. T. Uhl, J. R. Greer, and K. A. Dahmen, *Phys. Rev. Lett.* **109**, 095507 (2012).
  - [28] M. Zaiser, B. Marmo, and P. Moretti, in *Proceedings of Science 2005, International Conference on Statistical Mechanics of Plasticity and Related Instabilities*, PoS (SMPRI2005) 053.



- [29] O. L. Warren, S. A. Downs, and T. J. Wyrobek, *Z. Metallkd.* **95**, 287 (2004).
- [30] R. Maass and M. D. Uchic, *Acta Mater.* **60**, 1027 (2012).
- [31] J. R. Greer and J. T. M. De Hosson, *Prog. Mater. Sci.* **56**, 654 (2011).
- [32] S. Papanikolaou, F. Bohn, R. L. Sommer, G. Durin, S. Zapperi, and J. P. Sethna, *Nat. Phys.* **7**, 316 (2011).